

LOFAR Detection of a Low-Power Radio Halo in the Galaxy Cluster Abell 990

N. D. Hoang,¹★ T. W. Shimwell,^{2,3} E. Osinga,³ A. Bonafede,⁴ M. Brüggen,¹
A. Botteon,³ G. Brunetti,⁵ R. Cassano,⁵ V. Cuciti,¹ A. Drabent,⁶ C. Jones,⁷
H. J. A. Röttgering,³ and R. J. van Weeren³

¹*Hamburger Sternwarte, University of Hamburg, Gojenbergsweg 112, 21029 Hamburg, Germany*

²*Netherlands Institute for Radio Astronomy (ASTRON), P.O. Box 2, 7990 AA Dwingeloo, The Netherlands*

³*Leiden Observatory, Leiden University, PO Box 9513, NL-2300 RA Leiden, the Netherlands*

⁴*Department of physics and astronomy, Bologna University - Via Zamboni, 33, 40126 Bologna, Italy*

⁵*IRA INAF, via P. Gobetti 101 40129 Bologna, Italy*

⁶*Thüringer Landessternwarte, Sternwarte 5, 07778 Tautenburg, Germany*

⁷*Harvard-Smithsonian Center for Astrophysics, 60 Garden Street, Cambridge, MA 02138, USA*

Accepted 2020 November 13. Received 2020 October 15; in original form 2020 May 18

ABSTRACT

Radio halos are extended (\sim Mpc), steep-spectrum sources found in the central region of dynamically disturbed clusters of galaxies. Only a handful of radio halos have been reported to reside in galaxy clusters with a mass $M_{500} \lesssim 5 \times 10^{14} M_{\odot}$. In this paper we present a LOFAR 144 MHz detection of a radio halo in the galaxy cluster Abell 990 with a mass of $M_{500} = (4.9 \pm 0.3) \times 10^{14} M_{\odot}$. The halo has a projected size of ~ 700 kpc and a flux density of 20.2 ± 2.2 mJy or a radio power of $1.2 \pm 0.1 \times 10^{24}$ W Hz⁻¹ at the cluster redshift ($z = 0.144$) which makes it one of the two halos with the lowest radio power detected to date. Our analysis of the emission from the cluster with Chandra archival data using dynamical indicators shows that the cluster is not undergoing a major merger but is a slightly disturbed system with a mean temperature of 5 keV. The low X-ray luminosity of $L_X = (3.66 \pm 0.08) \times 10^{44}$ ergs s⁻¹ in the 0.1–2.4 keV band implies that the cluster is one of the least luminous systems known to host a radio halo. Our detection of the radio halo in Abell 990 opens the possibility of detecting many more halos in poorly-explored less-massive clusters with low-frequency telescopes such as LOFAR, MWA (Phase II) and uGMRT.

Key words: galaxies: clusters: individual (Abell 990) – galaxies: clusters: intra-cluster medium – large-scale structure of Universe – radiation mechanisms: non-thermal – diffuse radiation

1 INTRODUCTION

Diffuse (\sim Mpc) synchrotron radio emission (i.e. halos) in the centre of galaxy clusters indicates the presence of relativistic particles and large-scale magnetic fields in the intra-cluster medium (ICM). It is well known that the acceleration of particles to relativistic energy and the amplification of magnetic fields at these scales are associated with dynamical events in the host cluster of galaxies. However, the physical mechanisms governing the particle acceleration and the magnetic field amplification have not been fully understood (e.g., Brunetti & Jones 2014; van Weeren et al. 2019).

Radio halos are extended (\sim Mpc), faint ($\sim \mu$ Jy arcsec⁻² at

1.4 GHz), steep-spectrum¹ ($\alpha \lesssim -1$) sources that pervade large regions of the cluster. They are apparently unpolarised down to a few percent above ~ 1 GHz. In turbulent re-acceleration model (e.g. Brunetti et al. 2001; Petrosian 2001; Brunetti & Lazarian 2007), radio halos are generated by merger-induced turbulence that accelerates cosmic ray (CR) particles and/or amplifies the magnetic fields in the ICM. In addition, hadronic models that attempt to explain the generation of relativistic particles by the inelastic collisions between relativistic protons and thermal ions in the ICM seems to play a lesser role in the formation of radio halos (Ackermann et al. 2010; Brunetti & Jones 2014; Ackermann et al. 2016; Brunetti et al. 2017), but could be a more significant process in mini-halos that

★ E-mail: hoang@hs.uni-hamburg.de

¹ the convention $S \propto \nu^{\alpha}$ is used in this paper

have smaller sizes ($\lesssim 500$ kpc; Pfrommer & Enßlin 2004; Zandanel et al. 2014; Brunetti & Jones 2014).

Observational evidence shows that the generation of radio halos depends on the dynamical state of the host clusters and their mass (e.g. Wen & Han 2013; Cuciti et al. 2015). Radio halos are more likely to be observed in clusters that are massive and highly disturbed.

The power of radio halos is known to roughly correlate with their cluster mass and X-ray luminosities (e.g. Cassano et al. 2013; Bîrzan et al. 2019). The scatters in the correlations reflect the evolution of halos and dynamical state of clusters (e.g. Cuciti et al. 2015). Spectral properties of the halos are also a contributing factor to the scatters. According to turbulent re-acceleration models these properties reflect the efficiency of particle acceleration and are connected with cluster mass and dynamics. Steep spectrum halos are generally expected in less massive systems and at higher redshift, and are thought to be less powerful sitting below the radio power - cluster mass correlation (e.g. Cassano et al. 2006, 2010b, 2013; Brunetti et al. 2008).

Our understanding of the formation of radio halos are mainly based on studies of galaxy clusters that are more massive than $5 \times 10^{14} M_{\odot}$. There have been only a handful of radio halos detected in clusters that are less massive than $5 \times 10^{14} M_{\odot}$ (Abell 545, Giovannini et al. 1999; Bacchi et al. 2003; Abell 141 Duchesne et al. 2017; Abell 2061, Rudnick & Lemmerman 2009; Abell 2811, Duchesne et al. 2017; Abell 3562, Venturi et al. 2000, 2003; Giacintucci et al. 2005; PSZ1 G018.75+23.57, Bernardi et al. 2016; RXC J1825.3+3026, Botteon et al. 2019; Abell 2146, Hlavacek-Larrondo et al. 2018; Hoang et al. 2019). This is due to the sensitivity limitation of previous radio observations that are unable to detect faint radio halos in low-mass clusters. As a consequence, radio halos in the regime of low-mass clusters are largely unexplored. Steep-spectrum nature of radio halos makes low-frequency telescopes such as LOw Frequency ARray (LOFAR; Haarlem et al. 2013) ideal instruments for studying radio halos in the low-mass regime.

In this paper, we present our search for extended radio emission from the galaxy cluster Abell 990 (hereafter A990). With a mass of $M_{500} = (4.9 \pm 0.3) \times 10^{14} M_{\odot}$ (Planck Collaboration et al. 2016), A990 is an excellent target to search for cluster-scale radio emission in a mass range that is below the typical one where radio halos are found. We make use of the LOFAR Two-metre Sky Survey (LoTSS; Shimwell et al. 2017, 2019) 120 – 168 MHz data. The Karl G. Jansky Very Large Array (VLA) 1 – 2 GHz data and the archival NRAO VLA Sky Survey (NVSS) 1.4 GHz data are used to constraint the spectral properties the extended radio sources. In addition, we also use the archival X-ray Chandra data (Obs ID: 15114) to study dynamical state of the cluster.

We assume a flat Λ CDM cosmology with $\Omega_M = 0.3$, $\Omega_{\Lambda} = 0.7$, and $H_0 = 70 \text{ km s}^{-1} \text{ Mpc}^{-1}$. With the adopted cosmology, $1'$ corresponds to a physical size of 151.6 kpc at the cluster redshift, i.e. $z = 0.144$. The luminosity distance to the cluster is $D_L = 682.1 \text{ Mpc}$.

2 OBSERVATIONS AND DATA REDUCTION

2.1 LOFAR data

LoTSS is an on-going 120–168 MHz survey of the entire northern hemisphere (Shimwell et al. 2017, 2019). As of 4th March 2020, 1522 of 3168 pointings have been observed. The calibrated data

covering 27 percent of the northern sky will be released in the upcoming Data Release 2. A990 was observed with LOFAR, as part of LoTSS, during Cycle 4 and is covered by three pointings: P154+50, P156+47 and P158+50. Details of the observations are given in Table 1.

The LOFAR data was calibrated in two steps to correct for the direction-independent and direction-dependent effects using Prefactor² (van Weeren et al. 2016; Williams et al. 2016; de Gasperin et al. 2019) and ddf – pipeline³ (Tasse 2014a,b; Smirnov & Tasse 2015; Tasse et al. 2018; Shimwell et al. 2019), respectively. We briefly outline the procedure below. For a full description of the procedure, we refer to Shimwell et al. (2019).

In the direction-independent calibration, the absolute amplitude is corrected according to the Scaife & Heald (2012) flux scale. The calibration solutions are derived from the observations of 3C 196 which model has a total flux density of 83.1 Jy at 150 MHz. The initial XX-YY phase and clock offsets for each station are derived from the amplitude calibrator and are transferred to the target data. The target data are flagged and corrected for ionospheric Faraday rotation⁴. During the data processing, the radio frequency interference (RFI) is removed with AOF1agger (Offringa et al. 2012) when needed. The data are then phase calibrated against a wide-field sky model that is extracted from the GMRT 150 MHz All-sky Radio Survey (TGSS-ADR1) catalogue (Intema et al. 2017).

The direction dependent calibration step mainly aims to correct for the directional phase distortions caused by the ionosphere and the errors in the primary beam model of the LOFAR High Band Antennas (HBA). The direction dependent corrections are solved for each antenna in kMS⁵ (Tasse 2014a,b; Smirnov & Tasse 2015) implemented in the ddf – pipeline. The flux densities of the LOFAR detected sources are corrected with the bootstrapping technique using the VLSSr and WENSS catalogues (Hardcastle et al. 2016). Prior to the bootstrapping, the WENSS catalogue is scaled by a factor of 0.9 to be consistent with the flux density scale in LoTSS (i.e. Scaife & Heald 2012). To improve the image quality, the pipeline uses a “lucky imaging” technique that generates additional weights to the visibilities basing on the quality of the calibration solutions (Bonnassieux et al. 2018). For imaging, DDFacet imager (Tasse et al. 2018) is used to deconvolve the calibrated data on each facet.

To improve the quality of the final images in the cluster region, the data are processed through “extraction” and self-calibration steps. In the extraction, all sources outside of the cluster region are subtracted because they are not of the interest of this work. The sources outside of a $40' \times 40'$ box centred at the cluster are subtracted using the directional calibration solutions from the ddf – pipeline run. After the subtraction, data from all pointings are phase-shifted to the cluster position, averaged in time and frequency, and compressed with Dysco (Offringa 2016) to reduce data size. The data are corrected for the primary beam attenuation in the direction of the cluster by multiplying with a factor that is inversely proportional to the station beam response. The requirement for the beam correction here is that the region of interest (i.e. the angular size of the cluster) is small enough for the station beam response to be approximately uniform. In addition, the total flux density in the extraction region should be above ~ 0.3 Jy for the calibration to be converged. Details

² <https://www.astron.nl/citt/prefactor>

³ <https://github.com/mhardcastle/ddf-pipeline>

⁴ <https://github.com/lofar-astron/RMextract>

⁵ <https://github.com/saopicc/killMS>

Table 1. Observation details

Telescope	LOFAR 144 MHz ^a	VLA 1.5 GHz
Project/Pointing	LC4_034/P154+50, P156+47, P158+50	15A-270
Configurations	HBA_DUAL_INNER	B
Observing dates	Aug. 08, Jul. 21, Jun. 08, 2015	Feb. 22, 2015
Obs. IDs	L345594, L351840, L345592	-
Calibrators	3C 196	3C 196, 3C 286
Frequency (MHz)	120 – 168	1000 – 2000
Bandwidth (MHz)	48	1000
On-source time (hr)	24	0.6
Integration time (s)	1	3
Frequency resolution (kHz)	12.2	1000
Correlations	XX, XY, YX, YY	RR, RL, LR, LL
Number of stations/antennas	59, 60, 59	26

Notes: ^a for a detail description of the LoTSS data, see [Shimwell et al. 2017, 2019](#).

Table 2. Imaging parameters.

Data	uv -range (k λ)	Robust ^a (uv – taper)	θ_{FWHM} ('' \times '', PA^b)	σ ($\mu\text{Jy beam}^{-1}$)
LOFAR	0.15 – 65	–0.25 (5'')	16.6 \times 8.9 (84°)	80
	0.15 – 65	0.25 (10'')	60.4 \times 46.7 (–73°)	180
VLA	0.52 – 74.6	0.25 (10'')	10.9 \times 8.6 (68°)	38

Notes: ^a: Briggs weighting of the visibility. ^b: position angle.

of the “extraction” and self-calibration steps are described in [van Weeren et al. \(2020\)](#).

The combined data sets are processed with multiple self-calibration iterations including ‘tecandphase’ and gain calibration rounds. After each iteration, the calibration solutions are smoothed with LoSoTo⁶ ([de Gasperin et al. 2019](#)) to minimize the effect of noisy solutions. The final intensity images of the cluster at different resolution are created using WSClean⁷ ([Offringa et al. 2014](#)) with the imaging parameters in Table 2. To enhance extended sources, we subtract compact sources from the uv data and make images of the cluster with more weightings on the short uv baselines. The models for compact sources used in the subtraction are obtained from re-imaging the cluster using only data with uv distance longer than $1.0 k\lambda$, which do not contain extended emission larger than $4.2'$ (i.e. 637 kpc at the cluster redshift).

To examine the flux scale in the LOFAR images, we compare the flux densities of nearby compact sources with those in the TGSS-ADR1 150 MHz survey ([Intema et al. 2017](#)). The selected sources have a flux densities above 20σ in both LOFAR and TGSS-ADR1 images. We found that the flux scale in our LOFAR image is about 4 percent higher than the scale in the TGSS-ADR1 image. We adapt in our analysis a flux scale uncertainty of 10 percent.

2.2 VLA data

The VLA L band (1 – 2 GHz) data was taken on February 22, 2015 while the telescope was in the B-array configuration. The target was

observed for four scans of approximately ten minutes each, with a few hours in between the scans. The calibration is processed in the standard fashion (flux, phase, amplitude, band-pass etc.) with CASA⁸ using 3C 147 and 3C 286 as calibrators. The flux density scale was set according to the [Perley & Butler \(2017\)](#) flux scale. The RFI was automatically removed by the CASA ‘tfcrop’ and ‘flagdata’ tasks. To eliminate the remaining RFI after the CASA flaggers, the aoflagger ([Offringa et al. 2012](#)) was employed. Additionally, outlier visibilities were looked for in the amplitude- uv distance plane by inspecting the cross-hand (RL, LR) correlations. Since most radio sources are generally not polarised, the cross-hand correlations are a good additional indicator of RFI. In this plane, visibilities more than 6σ away from the mean were flagged.

Finally, to remove residual amplitude and phase errors and increase the quality of the image, we performed self-calibration of the target field. Three rounds of phase calibration and three rounds of amplitude and phase calibration with the decrease of the solution interval each round were done. Amplitude solutions with a signal-to-noise ratio smaller than three were flagged, as well as outlier ($> 3\sigma$ away from mean) amplitude solutions. The remaining RFI is manually flagged before the calibrated data is imaged with WSClean ([Offringa et al. 2014](#)). The final images are corrected for the attenuation of the primary beam by dividing the image pixel values by the VLA primary beam model created by CASA.

2.3 Chandra data

Chandra observations of A990 were performed for 10 ks on June 03, 2013 with the AXAF CCD Imaging Spectrometer (ObsID: 15114). The data were calibrated using the ClusterPyXT automatic pipeline⁹ ([Alden et al. 2019](#)) that calls pre-built routines in CIAO¹⁰ ([Fruscione et al. 2006](#)) and Sherpa¹¹ ([Freeman et al. 2001](#)). The pipeline is able to generate X-ray surface brightness, spectral temperature, pressure, particle density, and entropy maps from Chandra observations with minimal inputs from users. The pipeline retrieves the data and corresponding backgrounds from the Chandra data archive. As our interest is X-ray extended emission from the cluster, point sources are manually removed from the data. High

⁶ <https://github.com/revoltek/losoto>

⁷ <https://gitlab.com/aroffringa/wsclean>

⁸ <https://casa.nrao.edu>

⁹ <https://github.com/bcalden/ClusterPyXT>

¹⁰ <https://cxc.harvard.edu/ciao>

¹¹ <https://cxc.cfa.harvard.edu/sherpa/>

energy events are identified and filtered out by the pipeline. The gas temperature and pressure are obtained by spectral fitting of the events in the regions of interest. `ClusterPyXT` uses Astronomical Plasma Emission Code (APEC) model for optically thin collisionally ionized host plasma and a photoelectric absorption model (i.e. X-Spec PHABS) that includes redshift, metallicity, temperature, normalization and hydrogen column density along the line of sight (Balucinska-Church & McCammon 1992; Smith et al. 2001). We use a metallicity of $0.3 Z_{\odot}$ (e.g. Werner et al. 2013) and a hydrogen column density of $1.31 \times 10^{20} \text{ cm}^{-2}$ (Ben Bekhti et al. 2016) for the ICM. For details of the reduction procedure, we refer to Alden et al. (2019).

3 RESULTS

3.1 Radio emission

In Figure 1 we present the LOFAR 144 MHz radio emission contour maps of A990 at high and low resolution (see Table 2 for the image properties). The high-resolution contours show the detection of radio emission from galaxies which are labelled in Figure 2. The radio emission from the brightest cluster galaxy (BCG; at $\alpha = 10^{\text{h}}23^{\text{m}}39.9^{\text{s}}$, $\delta = +49^{\circ}08'38.4''$ and redshift $z_{sp} = 0.14216 \pm 0.00005$; Alam et al. 2015) is also seen in the high-resolution image. Due to the low surface brightness of the cluster-scale emission, it is only seen in the low-resolution contours. In the subsections below, we present measurements for the detected sources.

3.1.1 Extended radio source

Figure 1 shows that the extended radio emission is detected in the cluster centre, and its morphology is mainly extended in the NW–SE direction. The minimum and maximum projected sizes within the 3σ contour are 515 kpc and 960 Mpc, respectively. The projected size of the extended source is approximated as $D = \sqrt{515 \text{ kpc} \times 960 \text{ kpc}} \approx 700 \text{ kpc}$. The location and size of the extended source that mostly overlays the X-ray extended emission suggest that it is a radio halo.

The integrated flux density for the radio halo measured in the LOFAR low-resolution map is $S_{144 \text{ MHz}} = 20.2 \pm 2.2 \text{ mJy}$. Here we select only pixels that are detected with $\geq 3\sigma$ in the elliptical region in Figure 2. We did not integrate the emission in the region of source G and H as this is likely the residuals of the imperfect subtraction of these sources. The error takes into account the image noise and the flux scale uncertainty of 10 percent which are added in quadrature. The corresponding 144 MHz power for the radio halo at $z = 0.144$ is $P_{144 \text{ MHz}} = (1.2 \pm 0.1) \times 10^{24} \text{ W Hz}^{-1}$ (k -corrected, assuming a spectral index of $\alpha = -1.3$, i.e. the mean indices for a number of known halos, Feretti et al. 2012). To the best of our knowledge, A990 hosts one of the lowest radio power halos at low ($\leq 300 \text{ MHz}$) frequencies known to date (together with RXC J1825.3+3026 studied by Botteon et al. 2019). If the halo has a steep spectrum, $\alpha \lesssim -1.3$, the radio power at 1.4 GHz is $P_{1.4 \text{ GHz}} \lesssim (6.1 \pm 0.7) \times 10^{22} \text{ W Hz}^{-1}$ which is still being one of the lowest powers for a radio halo at 1.4 GHz (Botteon et al. 2019; Bîrzan et al. 2019). When all pixels above 2σ are included, the values increase by about 12 percent to $S_{144 \text{ MHz}} = 22.7 \pm 2.4 \text{ mJy}$ and $P_{144 \text{ MHz}} = (1.3 \pm 0.1) \times 10^{24} \text{ W Hz}^{-1}$. A similar difference in the flux density measurements within 2σ and 3σ contours was also seen in PSZ2 G099.86+58.45 (i.e. 15 percent; Cassano et al. 2019).

In this paper, we adopt the flux density measured with the $\geq 3\sigma$ pixels for the radio halo in A990 (i.e. $S_{144 \text{ MHz}} = 20.2 \pm 2.2 \text{ mJy}$).

The radio halo is undetected in the NVSS and VLA high-frequency images in Figure 3. The non-detection could be due to the sensitivity of the NVSS and VLA data. To examine this possibility, we compute the expected surface brightness at 1.4 GHz and 1.5 GHz, and compare it with the measurements in the NVSS and VLA images. Using the flux density measurement from the LOFAR data, we estimate the flux densities for the halo to be $S_{1.4 \text{ GHz}} = 2.1 \text{ mJy}$ and $S_{1.5 \text{ GHz}} = 2.0 \text{ mJy}$. Here we assume a flat spectrum, $\alpha = -1.0$, for the halo. This is a conservative approach as radio halos are generally found to have steeper spectra ($\bar{\alpha} \approx -1.3$; Feretti et al. 2012). The true flux densities of the halo at 1.4 GHz and 1.5 GHz could be lower than these estimates (e.g. with $\alpha = -1.3$, $S_{1.4 \text{ GHz}} = 1.1 \text{ mJy}$ and $S_{1.5 \text{ GHz}} = 1.0 \text{ mJy}$). To calculate the expected surface brightness of the halo, we assume that the halo emission is uniformly distributed over the source area. Hence, the surface brightness is $I_{1.4 \text{ GHz}} = S_{1.4 \text{ GHz}}/A = 0.035 \mu\text{Jy arcsec}^{-2}$ and $I_{1.5 \text{ GHz}} = 0.033 \mu\text{Jy arcsec}^{-2}$, where $A = 61,075 \text{ arcsec}^2$ is the area of the halo (i.e. covered by the $\geq 3\sigma$ in the LOFAR map). However, the sensitivity for the NVSS and VLA images is $\sigma = 0.20 \mu\text{Jy arcsec}^{-2}$ (Condon et al. 1998) and $\sigma = 0.36 \mu\text{Jy arcsec}^{-2}$ (see Table 2), respectively. These are not sensitive enough to detect the halo in A990. However, the radio emission at 144 MHz is not constant over the halo (Figure 3). The surface brightness emission at the peak region is ~ 1.7 times the mean pixel value in the halo region. In case that the emission at 1.4 GHz and 1.5 GHz follows the similar structure at 144 MHz, the surface brightness in some regions of the halo is expected to be higher, i.e. up to $0.06 \mu\text{Jy arcsec}^{-2}$ and $0.05 \mu\text{Jy arcsec}^{-2}$, respectively. The expected surface brightness is still below the detection limit of the NVSS and VLA observations. We also note that the NVSS and VLA observations are not ideal for detecting faint, extended emission at the scales of the cluster. The NVSS data obtained from snapshot observations is poorly sampled in the uv space. The VLA 1.5 GHz observations in B configuration is also lacking of short baselines. To estimate the halo spectrum, future deep observations at high frequencies with the VLA (e.g. C, D configuration) and uGMRT or at low frequencies with LOFAR Low Band Antennas (10–80 MHz) will be necessary.

3.1.2 Compact radio sources

A number of compact radio sources are detected with our LOFAR observations in Figure 1. In Table 3 we give the flux densities and spectra between 144 MHz and 1.5 GHz for the sources within a field of view of $\sim 10'$ centred on the cluster. The spectral indices of the compact sources range from -0.50 to -1.84 . The redshifts of sources B, D, K, and P range from 0.1326 to 0.15073 implying that they are at similar redshifts of the cluster members ($\bar{z} = 0.144$). The overlaid radio-SDSS optical images of the compact sources are shown in Figure A1. Sources A, E, G, H, I, L, and N do not have clear SDSS optical counterparts. Sources A and B consist of multiple point sources. Sources G and H are likely two lobes of a FR-I type active galactic nucleus.

3.2 X-ray emission

The Chandra 0.5 – 2.0 keV image of the cluster is shown in Figure 4. The X-ray emission from the cluster is relatively concentrated in the central region. Its peak emission is closed to the location of the BCG. In the outskirts, the X-ray emission has a lower surface brightness and is elongated in the NE–SW direction, which

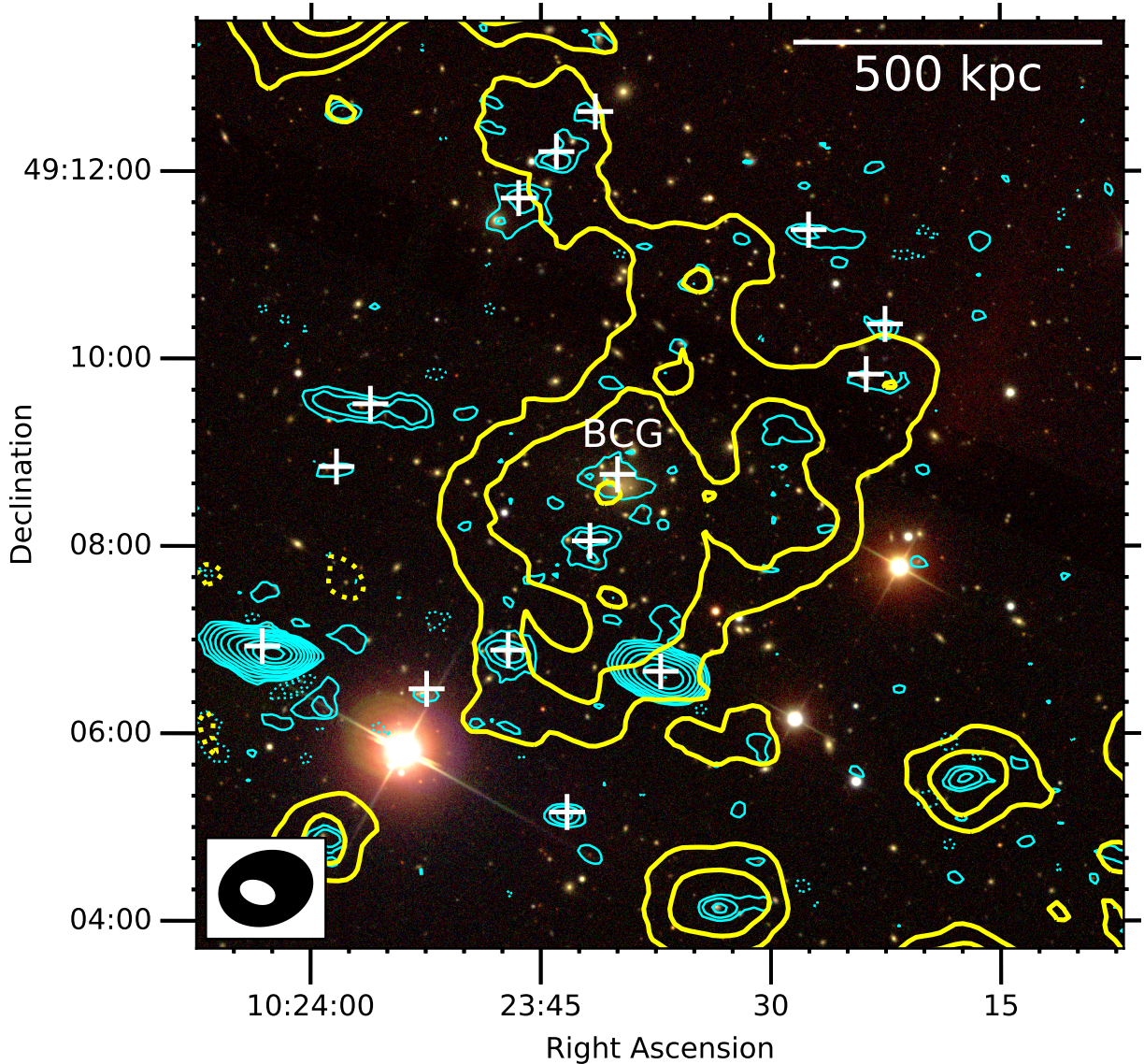


Figure 1. LOFAR 144 MHz high- ($16.6'' \times 8.9''$, cyan) and low- ($60.4'' \times 46.7''$, yellow) resolution contours on the SDSS optical (i, r, and g band) image. The contours are drawn at levels of $\pm[1, 2, 4, 8, 16, 32] \times 3\sigma$, where $\sigma = 80 \mu\text{Jy beam}^{-1}$ and $\sigma = 180 \mu\text{Jy beam}^{-1}$ for the high- and low-resolution contours, respectively. Negative contours are shown by the dotted lines. Compact sources including the BCG marked with the plus (+) are subtracted in the low-resolution contours. The synthesis beams are shown in the bottom left corner. Source labels are given in Figure 2.

is perpendicular to the major axis of the LOFAR 144 MHz radio emission. In the NE peripheral region of the cluster, X-ray emission is found, but radio emission is not detected. Reversibly, extended radio emission is detected in the west side of the cluster without X-ray emission seen. The total X-ray luminosity between energy range 0.1 keV and 2.4 keV within an elliptical region in Figure 4 is $L_X = (3.66 \pm 0.08) \times 10^{44} \text{ ergs s}^{-1}$, implying that A990 is one of the lowest X-ray luminosity clusters ever found to host a radio halo (Birzan et al. 2019). In the energy range 0.5–2.0 eV, the X-ray luminosity is $L_X = (2.45 \pm 0.06) \times 10^{44} \text{ ergs s}^{-1}$. The elliptical region is chosen to roughly cover the X-ray 3σ contours (i.e. $\sigma = 1.5 \times 10^{-9} \text{ counts cm}^{-2} \text{ s}^{-1}$). At the measured X-ray luminosity the cluster is about 8 times underluminous in the radio power compared with the $L_X - P_{1.4 \text{ GHz}}$ correlation (e.g. Cassano et al. 2013).

To study dynamical status of the cluster, we use the X-ray

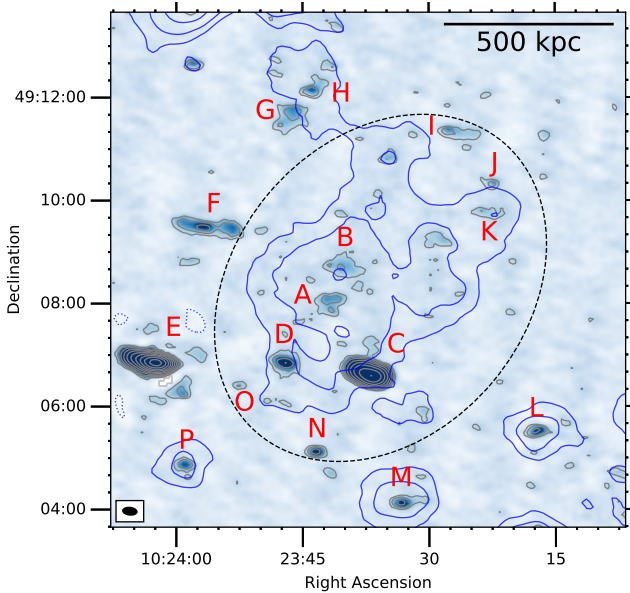
data to derive morphological indicators and to construct a cluster temperature map.

3.2.1 Dynamical status

Morphological properties of X-ray emission are known to correlate with dynamical state of the host clusters of galaxies (e.g. Cassano et al. 2010b; Bonafede et al. 2017). The X-ray emission from A990 in Figure 4 is mostly concentrated in the central region and is slightly elongated in the NE–SW direction which seems to indicate a slightly disturbed cluster but without major merging activities. We estimate a set of parameters to classify the merging status. These include (i) the concentration of the X-ray emission c (Santos et al. 2008), (ii) the centroid shifts between the X-ray emission peak and the centroid of the X-ray emission within aperture sizes (e.g. Poole et al. 2006), and (iii) the power ratios P_m/P_0 ($m = 3$; Buote & Tsai 1995). These are briefly described below.

Table 3. Flux densities and spectra for radio compact sources.

Source	$S_{144\text{ MHz}}$ [mJy]	$S_{1.4\text{ GHz}}$ [mJy]	α	z
A	1.77 ± 0.19	0.04 ± 0.04	-1.66 ± 0.41	–
B	1.79 ± 0.20	–	–	0.14216 ± 0.00005^a
C	75.10 ± 7.51	4.27 ± 0.22	-1.26 ± 0.05	0.6283 ± 0.0356^a
D	3.07 ± 0.32	0.34 ± 0.04	-0.97 ± 0.07	0.1326 ± 0.027^a
E	255.57 ± 25.46	34.74 ± 1.74	-0.88 ± 0.05	–
F	3.08 ± 0.32	0.44 ± 0.04	-0.86 ± 0.06	0.5383 ± 0.0303^a
G	2.33 ± 0.25	0.71 ± 0.05	-0.53 ± 0.06	–
H	1.26 ± 0.15	0.18 ± 0.04	-0.87 ± 0.11	–
I	1.31 ± 0.15	0.01 ± 0.04	-2.18 ± 1.81	–
J	0.44 ± 0.09	–	–	0.6717 ± 0.0655^a
K	0.59 ± 0.10	–	–	0.1326 ± 0.0364^a
L	1.24 ± 0.15	0.24 ± 0.04	-0.73 ± 0.09	–
M	1.52 ± 0.17	0.02 ± 0.04	-1.88 ± 0.79	0.1219 ± 0.0206^a
N	1.08 ± 0.13	0.14 ± 0.04	-0.92 ± 0.14	–
O	0.24 ± 0.08	0.21 ± 0.04	-0.06 ± 0.17	0.095 ± 0.0481^a
P	0.93 ± 0.12	–	–	0.15073 ± 0.00012^b

References: ^a: Alam et al. (2015); ^b: Rines et al. (2013).**Figure 2.** LOFAR 144 MHz high-resolution image of A990. The high-(gray) and low-(blue) resolution contours are the same as those in Figure 1. The ellipse is the region where the flux density of the halo is integrated. Compact sources are labelled.

i. Concentration of X-ray emission is defined as $c = S_X(r_1 < 100 \text{ kpc}) / S_X(r_2 < 500 \text{ kpc})$, where $S_X(r_i)$ is the total X-ray surface brightness within radius r_i .

ii. Centroid shift $w = SD[\Delta_i(r_i)] / R_{\text{ap}}$, where Δ_i is the projected separation between the X-ray emission peak and the centroid of the i^{th} aperture of radius r_i .

iii. Power ratio P_m/P_0 presents the fraction of the m^{th} multipole moment to the total power gravitational potential. The lowest power ratio moment with $m = 3$ gives a measure of the cluster substructures (e.g. Böhringer et al. 2010). For detailed formula, we refer to Buote & Tsai (1995).

Several studies have used these morphological parameters to

constrain the dynamical state of galaxy clusters (e.g. Böhringer et al. 2010; Cassano et al. 2010b; Bonafede et al. 2017; Savini et al. 2019). Clusters that are dynamically disturbed and host radio halos have a low value of c , high values of w and P_3/P_0 (e.g. Cassano et al. 2010b; Cuciti et al. 2015), except some cases in Bonafede et al. (2014, 2015a).

Following the calculations in Cassano et al. (2010b); Bonafede et al. (2017), we estimate the morphological parameters for A990 to be $c = 0.18$, $w = 0.025$, and $P_3/P_0 = 2.17 \times 10^{-7}$. The X-ray emission peak used in the calculation is shown in Figure 4. The centroid shift is calculated for circular apertures within $R_{\text{ap}} = 500 \text{ kpc}$. The first aperture starts from $r_i = 0.05 R_{\text{ap}}$ and the next ones increase in steps of $0.05 R_{\text{ap}}$. The power ratio P_3/P_0 is also calculated out to a radius of R_{ap} . We add our results to the morphological parameter diagrams in Figure 6.

The morphological parameter diagrams in Figure 6 show that A990 is located in the morphologically disturbed quadrant separated by the medians of c , w , and P_3/P_0 calculated from a sample of 32 galaxy clusters with X-ray luminosity $L_X \geq 5 \times 10^{44} \text{ erg s}^{-1}$ and redshift $0.2 \leq z \leq 0.32$ (Cassano et al. 2010b). When adding more clusters from Bonafede et al. (2015b) and from double relics Bonafede et al. (2017), the medians are slightly shifted (see Figure 6) and the points for A990 are closed to the boundaries for disturbed and relaxed clusters. This is in line with the idea that radio halos are generated in disturbed galaxy clusters that supply energy via turbulence for the particle re-acceleration and magnetic field amplification/generation.

3.2.2 Temperature map

We use ClusterPyXT package to perform spectral fitting of the X-ray data and to produce temperature map in Figure 7. The temperature map shows that the ICM gas has a mean temperature of about 5 keV which is a moderate value for the known clusters (e.g. Frank et al. 2013; Zhu et al. 2016). Across the cluster, the distribution of the ICM gas temperature is patchy. The temperature is slightly higher in the NW region (i.e. $\sim 5.4 \text{ keV}$) than that in the SE region of the cluster (i.e. $\sim 5.1 \text{ keV}$). In the core region, the mean temperature is about 5.2 keV around the X-ray emission peak and slightly increases to 5.4 keV at the distance of 120 kpc. However,

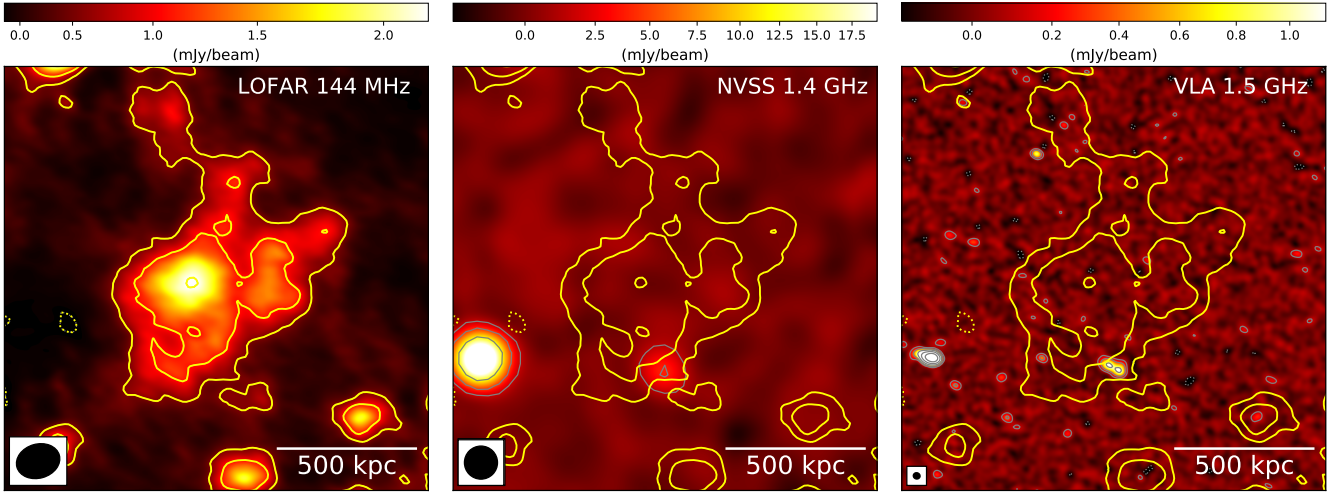


Figure 3. (From left to right) LOFAR 144 MHz, NVSS 1.4 GHz, and VLA 1.5 GHz image of A990. The NVSS and VLA (grey) contours are $\pm[1, 3, 9, 27, 81] \times 3\sigma$, where $\sigma = 450 \mu\text{Jy beam}^{-1}$ and $38 \mu\text{Jy beam}^{-1}$ for the NVSS and VLA images, respectively. The field of view of the images and the LOFAR low-resolution (yellow) contours without compact sources are the same as those in Figure 1.

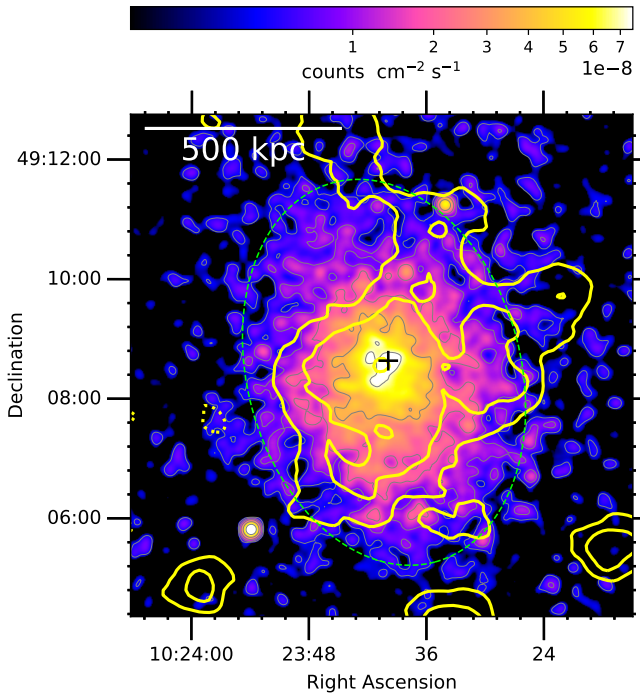


Figure 4. Chandra 0.5 – 2.0 keV image (bin=2) of the cluster overlaid with the LOFAR low-resolution contours. The Chandra data is smoothed with a Gaussian kernel of 5 pixels where the pixel size is $0.98''$. The X-ray emission peaks at the cross (+) location (RA = $10^{\text{h}}23^{\text{m}}39.9^{\text{s}}$ and Dec = $+49^{\text{d}}08^{\text{m}}38.4^{\text{s}}$). The ellipse used for X-ray luminosity measurement is centred at RA = $10^{\text{h}}23^{\text{m}}40.4^{\text{s}}$, Dec = $+49^{\text{d}}08^{\text{m}}25.7^{\text{s}}$ with a position angle of 15 degree. The major and minor axes are $4.58'$ and $6.57'$ (i.e. 694 kpc and 996 kpc), respectively.

these variations are still within the mean errors of ~ 0.55 keV (see Figure 7, right). This is due to the short exposure duration of the X-ray observations (i.e. 10 ks). Future deep X-ray observations will

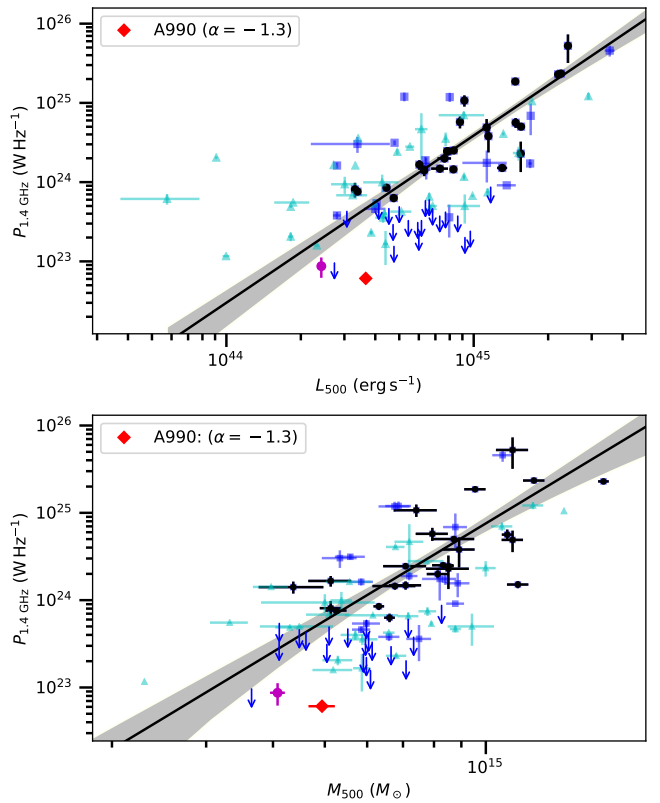


Figure 5. The $P_{1.4 \text{ GHz}} - M_{500}$ (bottom) and $P_{1.4 \text{ GHz}} - L_{500}$ (top) relations, adapted from Bîrzan et al. (2019). The data points for A990 and RXC J1825.3+3026 are shown by the red diamond and magenta circle, respectively. In both panels, the black circles, blue squares, and cyan triangles show radio halos in the samples of Cassano et al. (2013), Martínez Aviles et al. (2016), and Bîrzan et al. (2019), respectively. The blue arrows indicate the power upper limits for undetected halos in the Cassano et al. (2013), Kale et al. (2015), and Bîrzan et al. (2019) cluster samples. The solid lines are the best fits for the Cassano et al. (2013) halos. The shadowed regions show the 95 percent confidence region.

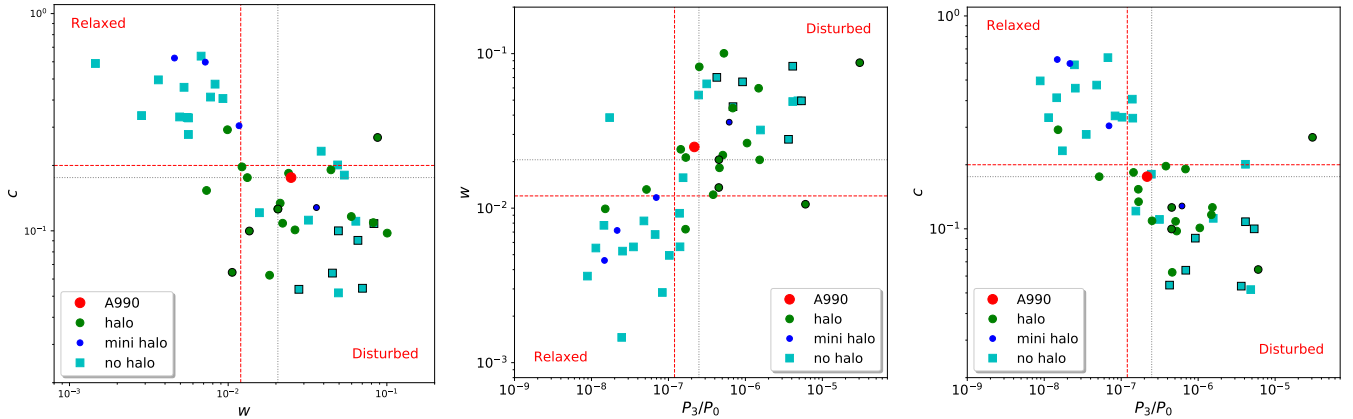


Figure 6. Morphological parameter diagrams for clusters with and without radio halos (Cassano et al. 2010b; Bonafede et al. 2014, 2017). Clusters with radio halos are shown with filled circles. Radio quiet clusters are plotted with cyan squares. Clusters hosting double relics are additionally marked with black circles. The data points for A990 are marked with the red circles. The red dashed lines indicate the median values (i.e. $c = 0.2$, $w = 0.012$, $P_3/P_0 = 1.2 \times 10^{-7}$) calculated from a complete sample of 32 galaxy clusters (Cassano et al. 2010b). The black dotted lines (i.e. $c = 0.18$, $w = 0.021$, $P_3/P_0 = 2.5 \times 10^{-7}$) are calculated for all clusters in the plots.

provide information on the possible temperature variations in the cluster.

4 DISCUSSION

We have reported the detection of an extended radio source in A990 and classify it as a radio halo. The classification is based on (i) its extended size of 700 kpc that is not associated with any compact sources, (ii) its location at the cluster centre, (iii) its extended emission largely overlaid the X-ray extended emission from the ICM. A990 with a mass of $M_{500} = (4.9 \pm 0.3) \times 10^{14} M_{\odot}$ (Planck Collaboration et al. 2016) is among the less massive clusters known to host a giant radio halo.

The power for radio halos is well known to correlate with the mass and X-ray luminosity of their host clusters (e.g. Cassano et al. 2013). To examine the correlations in case of A990, we add our data points to the existing $P_{1.4 \text{ GHz}} - M_{500}$ and $P_{1.4 \text{ GHz}} - L_{500}$ correlations (see Figure 5). Here L_{500} is the X-ray luminosity measured within a radius R_{500} at which the total particle density is 500 times the critical density of the Universe at the cluster redshift. If $\alpha = -1.0$, the radio power at 1.4 GHz is $P_{1.4 \text{ GHz}} = 1.2 \pm 0.1 \times 10^{23} \text{ W Hz}^{-1}$ which is well below the expected value for a cluster that has a mass of $(4.9 \pm 0.3) \times 10^{14} M_{\odot}$ (i.e. 5 times less power than expected) and X-ray luminosity of $(3.66 \pm 0.08) \times 10^{44} \text{ ergs s}^{-1}$ (i.e. 4 times underluminous in radio power). In case of $\alpha = -1.3$ (see Sec. 3.1), the halo power is lower, i.e. $P_{1.4 \text{ GHz}} = 6.1 \times 10^{22} \text{ W Hz}^{-1}$ and is significantly below the correlations (i.e. 9 and 8 times lower than expected from the $P_{1.4 \text{ GHz}} - M_{500}$ and $P_{1.4 \text{ GHz}} - L_{500}$ correlations, respectively) and the upper limit values for undetected halos (Figure 5). The difference could be that A990 lies in the poorly-constrained regions for less-massive clusters in the $P_{1.4 \text{ GHz}} - M_{500}$ and $P_{1.4 \text{ GHz}} - L_{500}$ correlations. However, it is still interesting that the halo in A990 is also about 3 times less powerful than the typical upper limits for halos that are thought to have ultra-steep spectra (i.e. blue arrows in Figure 5). Our morphological analysis of the cluster A990 with a mass of $(4.9 \pm 0.3) \times 10^{14} M_{\odot}$ and its position in the $P_{1.4 \text{ GHz}} - M_{500}$ and $P_{1.4 \text{ GHz}} - L_{500}$ diagrams suggest that A990 can possibly host a radio halo with an ultra-steep spectrum. However, adequate higher- or lower-frequency observations are necessary to constrain its spectrum and confirm the scenario.

In the turbulence re-acceleration model, radio halos are formed through merger induced turbulence and are likely to be detected in massive merging clusters. In these systems, a fraction of an amount of turbulent energy flux is channelled into the acceleration of relativistic particles and the amplification/generation of magnetic fields in the ICM during cluster mergers. In less-massive clusters, merging events inject less energy into the ICM, resulting in radio halos being formed less frequently and with steeper spectra (e.g. Brunetti et al. 2008; Cassano et al. 2010a, 2012). The model predicts that only about 10 – 15 percent of clusters with a mass below $6.5 \times 10^{14} M_{\odot}$ hosts Mpc-scale radio halos with spectra flatter than $\alpha \sim -1.5$ (e.g. Cuciti et al. 2015). At these masses, giant halos with steeper spectra are expected to be more common and the fraction of these clusters with halos increase up to 40 percent including steeper spectrum halos (e.g. Cassano et al. 2006, 2010a; Cuciti et al. 2015). Therefore, the detection of radio halos in clusters with $M_{500} \lesssim 6.5 \times 10^{14} M_{\odot}$ is expected to be more common at low frequencies with LOFAR (Haarlem et al. 2013), MWA (Phase II; Wayth et al. 2018), and uGMRT (Gupta et al. 2017). Our discovery of the radio halo in A990 with LOFAR and the fact that it sits below the correlations are in line with such expectations.

The low power of A990 in the $P_{1.4 \text{ GHz}} - M_{500}$ and $P_{1.4 \text{ GHz}} - L_{500}$ planes could also indicate a particular phase in the evolutionary state of the cluster. Magnetohydrodynamic (MHD) simulations of the re-acceleration of cosmic ray electrons by merger induced turbulence by Donnert et al. (2013) modelled the evolution of a radio halo power during cluster mergers. The radio halo becomes brighter after the merger and it is fainter in a later merging stage. At the same time the halo spectrum is flattened in the early stage of the merger, but is steepened below -1.5 after a few Gyrs of core passage. The halo could be observed for a few Gyrs depending on the observing frequencies which probe different energy of the population of relativistic electrons and magnetic field strength. At low frequencies, the halo is observable much longer due to the large lifetime of relativistic electrons with lower energy and weak magnetic fields.

In general, spectral information are thus crucial to understand the origin and evolution of radio halos. On-going radio surveys of a large fraction of the sky such as LoTSS (Shimwell et al. 2017, 2019) will provide statistical estimates on the fraction of

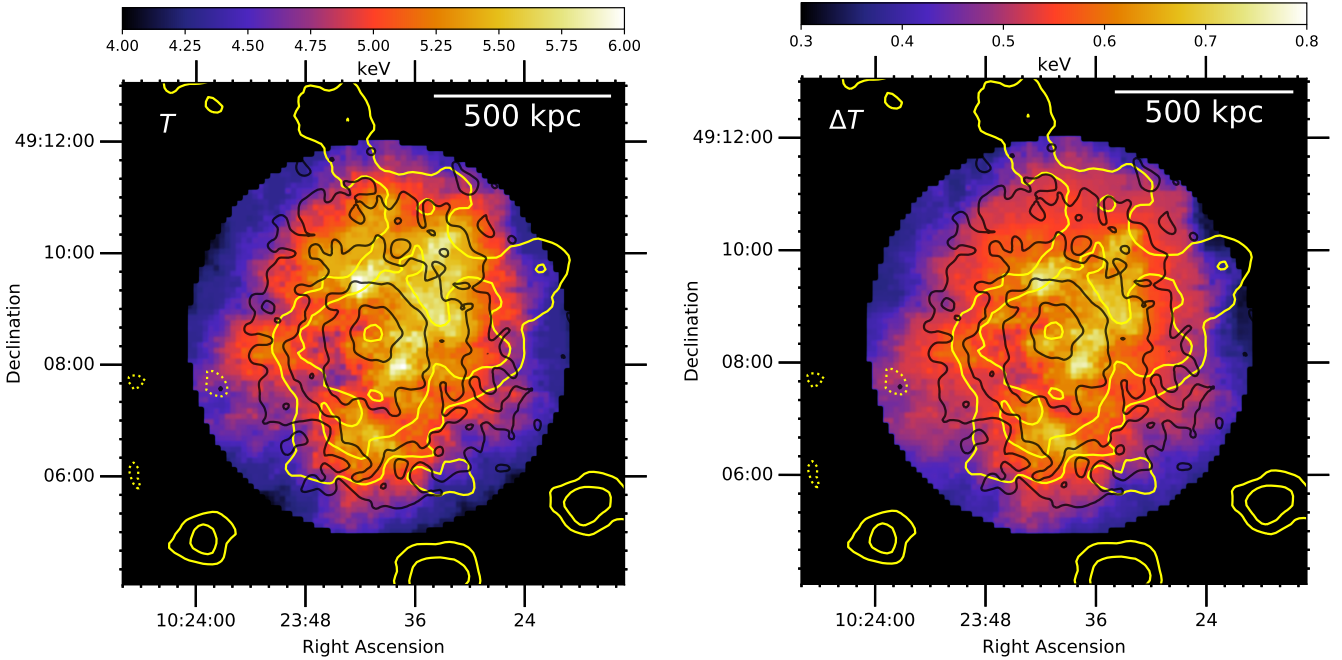


Figure 7. Temperature and error maps overlaid with the LOFAR low-resolution (yellow) and Chandra (black) contours. The contour levels are identical to those in Figure 4. The cluster has a mean temperature of 5 keV.

radio halos in complete samples of clusters down to relatively small masses. In combination with high-frequency observations with the ASKAP/EMU (e.g. clusters with declination between 0 and $+30^\circ$), uGMRT and VLA telescopes, the halo spectra will be measured which will improve our understanding of the mechanism of particle acceleration and magnetic field amplification/generation at cluster scales.

5 CONCLUSIONS

In this paper we present LOFAR 144 MHz observations, as part of the LoTSS surveys, of the galaxy cluster Abell 990 ($z = 0.144$) with a mass of $M_{500} = (4.9 \pm 0.3) \times 10^{14} M_\odot$. We detect an extended radio emission with a projected size of ~ 700 kpc at the cluster centre. Due to its location and size, we classify the extended radio emission as a radio halo.

The flux density at 144 MHz for the halo is $S_{144 \text{ MHz}} = 20.2 \pm 2.2$ mJy (i.e. above 3σ contours), corresponding to a radio power of $P_{144 \text{ MHz}} = (1.2 \pm 0.1) \times 10^{24} \text{ W Hz}^{-1}$ (k -corrected). The radio halo is one of the two lowest power radio halos detected to date.

Our analysis on the dynamical status of the cluster using the X-ray data reveals that the cluster has a slightly disturbed ICM and does not have major merger activities. The X-ray luminosity of the halo between 0.1–2.4 keV is $L_{500} = (3.66 \pm 0.08) \times 10^{44} \text{ ergs s}^{-1}$. The cluster mean temperature is relatively low, at 5 keV. There are possible variations in the temperature, but require deep X-ray observations to confirm.

Our measurements on the radio power, X-ray luminosity, and the ICM temperature are at the low ends. This can be explained by the cluster being a dynamically disturbed, less massive system that contains less energy than more massive clusters.

Our study reveals the potential of detecting many faint radio halos in less-massive galaxy clusters with LOFAR. With the full

coverage of the northern hemisphere, the LoTSS survey will provide the fraction of clusters of this mass hosting radio halos that will be compared with the theoretical predictions (e.g. [Cassano et al. 2010a](#)). A combination with high-frequency observations will provide spectral information on the sources that are important for studies of the origin of radio halos.

ACKNOWLEDGEMENTS

We thank the anonymous referee for the helpful comments. DNH and A.Bonafede acknowledge support from the ERC-Stg17 714245 DRANOEL. MB acknowledges support from the Deutsche Forschungsgemeinschaft under Germany's Excellence Strategy - EXC 2121 "Quantum Universe" - 390833306. A.Botteon, EO, and RJvW acknowledge support from the VIDI research programme with project number 639.042.729, which is financed by the Netherlands Organisation for Scientific Research (NWO). HR acknowledges support from the ERC Advanced Investigator programme NewClusters 321271. AD acknowledges support by the BMBF Verbundforschung under the grant 05A17STA : The Jülich LOFAR Long Term Archive and the German LOFAR network are both coordinated and operated by the Jülich Supercomputing Centre (JSC), and computing resources on the supercomputer JUWELS at JSC were provided by the Gauss Centre for supercomputing e.V. (grant CHTB00) through the John von Neumann Institute for Computing (NIC). These data were (partly) processed by the LOFAR Two-Metre Sky Survey (LoTSS) team. This team made use of the LOFAR direction independent calibration pipeline (<https://github.com/lofar-astron/prefactor>) which was deployed by the LOFAR e-infragroup on the Dutch National Grid infrastructure with support of the SURF Co-operative through grants e-infra 160022 e-infra 160152 (Mechev et al. 2017, PoS(ISGC2017)002). The LoTSS direction dependent calibration and imaging pipeline (<http://github.com/mhardcastle/ddf-pipeline>) was run

on compute clusters at Leiden Observatory and the University of Hertfordshire which are supported by a European Research Council Advanced Grant [NEWCLUSTERS-321271] and the UK Science and Technology Funding Council [ST/P000096/1]. We have including the lotss-dr2-infrastructure list as this project made use of the DR2 pipeline and post processing extraction/selfcal scheme. The scientific results reported in this article are based on data obtained from the Chandra Data Archive. This research has made use of software provided by the Chandra X-ray Center (CXC) in the application packages CIAO, ChIPS, and Sherpa. The National Radio Astronomy Observatory is a facility of the National Science Foundation operated under cooperative agreement by Associated Universities, Inc.

DATA AVAILABILITY

The data underlying this article will be shared on reasonable request to the corresponding author.

REFERENCES

- Ackermann M., et al., 2010, *ApJ*, 717, L71
- Ackermann M., et al., 2016, *ApJ*, 819, 149
- Alam S., et al., 2015, *Astrophys. Journal, Suppl. Ser.*, 219
- Alden B., Hallman E. J., Rapetti D., Burns J. O., Datta A., 2019, *Astron. Comput.*, 27, 147
- Bacchi M., Feretti L., Giovannini G., Govoni F., 2003, *A&A*, 400, 465
- Balucinska-Church M., McCammon D., 1992, *ApJ*, 400, 699
- Ben Bekhti N., et al., 2016, *A&A*, 594, A116
- Bernardi G., et al., 2016, *MNRAS*, 456, 1259
- Birzan L., et al., 2019, *MNRAS*, 487, 4775
- Böhringer H., et al., 2010, *A&A*, 514, A32
- Bonafede A., et al., 2014, *Mon. Not. R. Astron. Soc. Lett.*, 444, L44
- Bonafede A., et al., 2015a, *MNRAS*, 454, 3391
- Bonafede A., et al., 2015b, *MNRAS*, 454, 3391
- Bonafede A., et al., 2017, *MNRAS*, 470, 3465
- Bonnassieux E., Tasse C., Smirnov O., Zarka P., 2018, *A&A*, 615, A66
- Botteon A., et al., 2019, *A&A*, 630, A77
- Brunetti G., Jones T. W., 2014, *Int. J. Mod. Phys. D*, 23, 1430007
- Brunetti G., Lazarian A., 2007, *MNRAS*, 378, 245
- Brunetti G., Setti G., Feretti L., Giovannini G., 2001, *MNRAS*, 320, 365
- Brunetti G., et al., 2008, *Nature*, 455, 944
- Brunetti G., Zimmer S., Zandanel F., 2017, *MNRAS*, 472, 1506
- Buote D. A., Tsai J. C., 1995, *ApJ*, 452, 522
- Cassano R., Brunetti G., Setti G., 2006, *MNRAS*, 369, 1577
- Cassano R., Brunetti G., Röttgering H. J. A., Bruggen M., 2010a, *A&A*, 509, 68
- Cassano R., Etori S., Giacintucci S., Brunetti G., Markevitch M., Venturi T., Gitti M., 2010b, *ApJ*, 721, L82
- Cassano R., Brunetti G., Norris R., Röttgering H., Johnston-Hollitt M., Trasatti M., 2012, *A&A*, 548, A100
- Cassano R., et al., 2013, *ApJ*, 777, 141
- Cassano R., et al., 2019, *ApJ*, 881, L18
- Condon J. J., Cotton W. D., Greisen E. W., Yin Q. F., Perley R. A., Taylor G. B., Broderick J. J., 1998, *Astron. J.*, 115, 1693
- Cuciti V., Cassano R., Brunetti G., Dallacasa D., Kale R., Etori S., Venturi T., 2015, *A&A*, 580, A97
- Donnert J., Dolag K., Brunetti G., Cassano R., 2013, *MNRAS*, 429, 3564
- Duchesne S. W., Johnston-Hollitt M., Offringa A. R., Pratt G. W., Zheng Q., Dehghan S., 2017, 35, 1
- Feretti L., Giovannini G., Govoni F., Murgia M., 2012, *Astron. Astrophys. Rev.*, 20, 54
- Frank K. A., Peterson J. R., Andersson K., Fabian A. C., Sanders J. S., 2013, *ApJ*, 764, 46
- Freeman P., Doe S., Siemiginowska A., 2001, Sherpa: a mission-independent data analysis application. pp 76–87, doi:10.1117/12.447161, <http://proceedings.spiedigitallibrary.org/proceeding.aspx?articleid=892330>
- Fruscione A., et al., 2006, CIAO: Chandra's data analysis system. p. 62701V, doi:10.1117/12.671760, <http://proceedings.spiedigitallibrary.org/proceeding.aspx?doi=10.1117/12.671760>
- Giacintucci S., et al., 2005, *A&A*, 440, 867
- Giovannini G., Tordi M., Feretti L., 1999, *New Astron.*, 4, 141
- Gupta Y., et al., 2017, *Curr. Sci.*, 113, 707
- Haarlem M. P. V., et al., 2013, *A&A*, 2, 1
- Hardcastle M. J., et al., 2016, *MNRAS*, 462, 1910
- Hoang D. N., et al., 2019, *A&A*, 622, 1
- Hlavacek-Larrondo J., et al., 2018, *MNRAS*, 475, 2743
- Intema H. T., Jagannathan P., Mooley K. P., Frail D. A., 2017, *A&A*, 598, A78
- Kale R., Venturi T., Cassano R., Giacintucci S., Bardelli S., Dallacasa D., Zucca E., 2015, *A&A*, 581, A23
- Martinez Aviles G., et al., 2016, *A&A*, 595, A116
- Offringa A. R., 2016, *A&A*, 595, 1
- Offringa A. R., van de Gronde J. J., Roerdink J. B. T. M., 2012, *A&A*, 539, A95
- Offringa A. R., et al., 2014, *MNRAS*, 444, 606
- Perley R. A., Butler B. J., 2017, *Astrophys. J. Suppl. Ser.*, 230, 7
- Petrosian V., 2001, *ApJ*, 557, 560
- Pfrommer C., Enßlin T. A., 2004, *MNRAS*, 352, 76
- Planck Collaboration et al., 2016, *A&A*, 594, A27
- Poole G. B., Fardal M. A., Babul A., McCarthy I. G., Quinn T., Wadsley J., 2006, *MNRAS*, 373, 881
- Rines K., Geller M. J., Diaferio A., Kurtz M. J., 2013, *ApJ*, 767, 15
- Rudnick L., Lemmerman J. A., 2009, *ApJ*, 697, 1341
- Santos J. S., Rosati P., Tozzi P., Böhringer H., Etori S., Bignamini A., 2008, *A&A*, 483, 35
- Savini F., et al., 2019, *A&A*, 622
- Scaife A. M. M., Heald G. H., 2012, *Mon. Not. R. Astron. Soc. Lett.*, 423, 30
- Shimwell T. W., et al., 2017, *A&A*, 598, A104
- Shimwell T. W., et al., 2019, *A&A*, 622, A1
- Smirnov O. M., Tasse C., 2015, *MNRAS*, 449, 2668
- Smith R. K., Brickhouse N. S., Liedahl D. A., Raymond J. C., 2001, *ApJ*, 556, L91
- Tasse C., 2014a, ArXiv e-prints 1410.8706v1
- Tasse C., 2014b, *A&A*, 566
- Tasse C., et al., 2018, *A&A*, 611, 1
- Venturi T., Bardelli S., Morganti R., Hunstead R. W., 2000, *MNRAS*, 314, 594
- Venturi T., Bardelli S., Dallacasa D., Brunetti G., Giacintucci S., Hunstead R. W., Morganti R., 2003, *A&A*, 402, 913
- Wayth R. B., et al., 2018, *Publ. Astron. Soc. Aust.*, 35, e033
- Wen Z. L., Han J. L., 2013, *MNRAS*, 436, 275
- Werner N., Urban O., Simionescu A., Allen S. W., 2013, *Nature*, 502, 656
- Williams W. L., et al., 2016, *MNRAS*, 460, 2385
- Zandanel F., Pfrommer C., Prada F., 2014, *MNRAS*, 438, 124
- Zhu Z., et al., 2016, *ApJ*, 816, 54
- de Gasperin F., et al., 2019, *A&A*, 622, A5
- van Weeren R. J., et al., 2016, *Astrophys. J. Suppl. Ser.*, 223, 2
- van Weeren R. J., de Gasperin F., Akamatsu H., Brüggén M., Feretti L., Kang H., Stroe A., Zandanel F., 2019, *Space Sci. Rev.*, 215, 16
- van Weeren, R. J., Shimwell, T. W., Botteon, A., et al. 2020, ArXiv e-prints, arXiv: 2011.02387

APPENDIX A: OPTICAL COUNTERPARTS OF COMPACT SOURCES

To identify optical counterparts of the radio compact sources, we overlaid the LOFAR high-resolution contours on SDSS images in Figure [A1](#).

This paper has been typeset from a \LaTeX file prepared by the author.

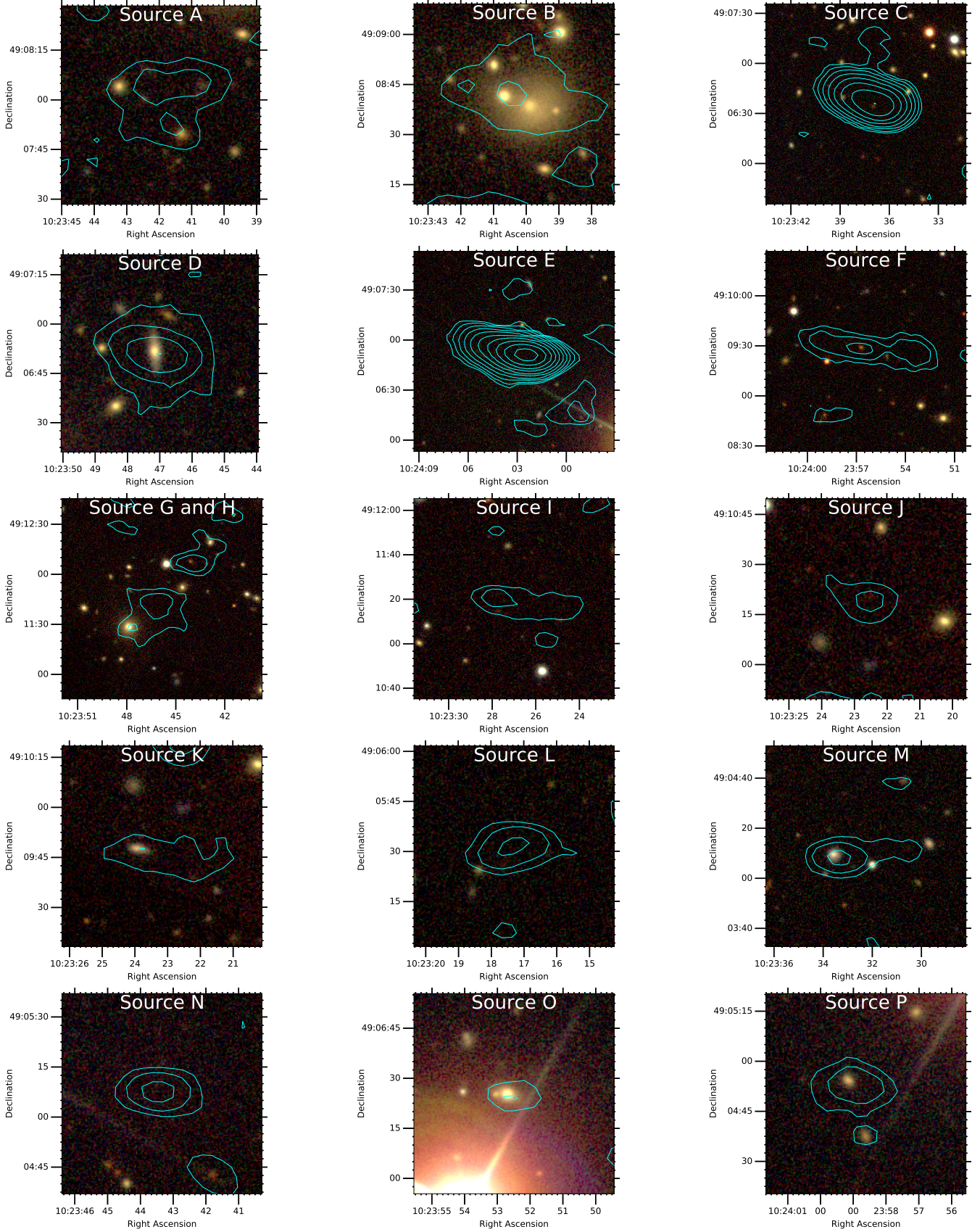


Figure A1. SDSS optical (i, r, and g band) images overlaid with the LOFAR high-resolution contours. The contours are at the same levels as those in Figure 1. The source labels are given in Figure 2.